Structural Dynamics of Myoglobin: Effect of Internal Cavities on Ligand Migration and Binding†

Karin Nienhaus,‡ Pengchi Deng,‡ Jan M. Kriegl,‡ and G. Ulrich Nienhaus*,‡,§

Department of Biophysics, University of Ulm, 89069 Ulm, Germany, and Department of Physics, University of Illinois at Urbana-Champaign, Urbana, Illinois 61801

Received May 14, 2003; Revised Manuscript Received June 21, 2003

ABSTRACT: Using Fourier transform infrared (FTIR) spectroscopy combined with temperature derivative spectroscopy (TDS) at cryogenic temperatures, we have studied CO binding to the heme and CO migration among cavities in the interior of sperm whale carbonmonoxy myoglobin (MbCO) after photodissociation. Photoproduct intermediates, characterized by CO in different locations, were selectively enhanced by laser illumination at specific temperatures. Measurements were performed on the wild-type protein and a series of mutants (L104W, I107W, I28F, and I28W) in which bulky amino acid side chains were introduced to block passageways between cavities or to fill these sites. Binding of xenon was also employed as an alternative means of filling cavities. In all samples, photolyzed CO ligands were observed to initially bind at primary docking site B in the vicinity of the heme iron, from where they migrate to the secondary docking sites, the Xe4 and/or Xe1 cavities. To examine the relevance of these internal docking sites for physiological ligand binding, we have performed room-temperature flash photolysis on the entire set of proteins in the CO- and O_2-bound form. Together with the cryospectroscopic results, these data provide a clear picture of the role of the internal sites for ligand escape from and binding to myoglobin.

After more than 40 years of intense research, the detailed mechanism of ligand binding to myoglobin (Mb)[1] resembles an unfinished puzzle. In recent years, X-ray structures of photoproduct intermediates of MbCO in which the CO is located in different hydrophobic cavities in the interior of the protein after dissociation from the heme iron have become available. Moreover, time-resolved crystallography has given direct structural evidence of CO migration in MbCO crystals at room temperature (*1*, *2*). Spectroscopic methods, however, can in principle provide better sensitivity, and in this paper, we will show that FTIR spectroscopy in the strong stretch bands of heme-bound and photodissociated CO is a superb tool for studying ligand migration and binding in heme proteins.

In the preceding paper (*3*), we have investigated ligand migration and binding in sperm whale myoglobin (Mb) mutant L29W. The L29W mutant is a modified protein with remarkable properties, most importantly, its slow ligand dissociation rate (*4*), which greatly facilitates enhancement of reaction intermediates after photolysis. With special illumination procedures at cryogenic temperatures and FTIR spectroscopy, pronounced spectral changes were observed in the bands of the CO stretch that were concomitant with changes in the temperature of rebinding. These effects were explained by CO migration between different internal docking sites in the protein as well as protein relaxation. A number of photoproduct intermediates (B, C′, C″, and D) were identified and assigned to structures previously measured with X-ray crystallography at cryogenic temperatures (*5*). To confirm the assignment of photoproduct states to structures with CO in specific locations, we had also introduced secondary mutations in the protein, in which internal cavities are blocked by bulky amino acid side chains.

Here we extend the investigation of photoproduct intermediates to wild-type (wt) sperm whale MbCO. For this protein, light-induced intermediate states were studied earlier with MbCO in solutions and crystals. In both types of samples, a number of discrete photoproduct states were observed (*6*, *7*). As yet, X-ray studies have only partially succeeded in assigning these states to specific structures with photolyzed ligands in certain docking sites. In 1994, the first photoproduct structures of wt MbCO were determined by X-ray diffraction below 40 K (*8*, *9*). They showed the photodissociated CO ligands in primary docking site B near the active site on top of the heme group, oriented parallel to the heme plane above pyrrol C. In horse heart myoglobin MbCO crystals, extended illumination at ∼160 K yielded a small fraction of CO molecules in the xenon 1 (Xe1) cavity (*10*). Using nanosecond time-resolved X-ray structure analysis on sperm whale MbCO, Moffat and co-workers have recently shown that the CO in the Xe1 site reached its highest occupancy at ∼100 ns and decayed to half of its peak value ∼10 μs after photolysis. Thereafter, the CO molecules disappeared from the electron density map and subsequently reappeared at the heme iron with a second-order rate coefficient of 4.5×10^5 M^{-1} s^{-1} (*2*).

† This work was supported by the Deutsche Forschungsgemeinschaft (Ni-291/3).

* To whom correspondence should be addressed. E-mail: uli@uiuc.edu.

‡ University of Ulm.

§ University of Illinois at Urbana-Champaign.

[1] Abbreviations: Mb, myoglobin; wt, wild type; FTIR, Fourier transform infrared; TDS, temperature derivative spectroscopy.

10.1021/bi034788k CCC: $25.00
Published on Web 07/23/2003

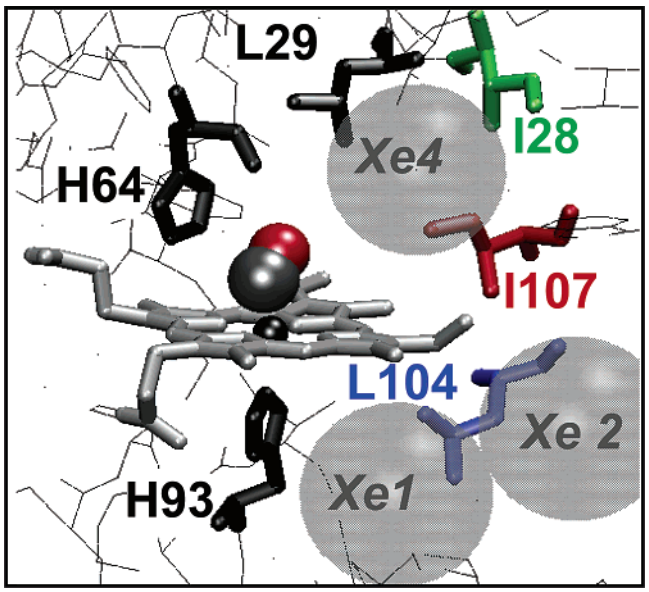

FIGURE 1: Essential features at the active site of wt MbCO with the CO bound to the heme iron. Residues that have been mutated in this work are depicted in color, and protein cavities are depicted as gray circles.

The description of ligand binding in wt MbCO presented above is somewhat simplified because discrete bound state conformations (taxonomic substates) exist, and each of them has its individual set of photoproduct intermediates. The major substates A_0, A_1, and A_3 are associated with IR bands at 1966, 1945, and 1927 cm^{-1}, respectively (*4*, *11*−*16*). The dispersion of the CO stretch absorption into a small number of A substate bands is caused by electrostatic interactions between the CO dipole and the imidazole side chain of the distal histidine, H64, which can assume different conformations (*4*, *17*−*20*). At low pH, the imidazole side chain is protonated and swings toward the solvent to better solvate its charge. The resulting "open" conformation is associated with A_0, whereas the "closed" conformation is related to A_1 and A_3 (*21*, *22*). In 1999, Vojtechovsky *et al.* (*23*) refined their 1.2 Å X-ray structure of MbCO with multiple occupancies of H64 and obtained, besides an occupancy of 20% for A_0, two slightly different positions of the imidazole side chain inside the pocket, occupied to 60 and 20%. They assigned these two conformations to A_1 and A_3, with the distal histidine positioned deeper in the distal pocket in A_3. This assignment is supported by kinetic studies of A substate interconversions: exchange between A_1 and A_3 is orders of magnitude faster than the A_1/A_3 exchange with A_0, which suggests that the former involves smaller structural changes than the latter (*15*).

In this work, we have studied ligand migration and binding using FTIR−TDS experiments with wt MbCO and mutants L104W, I107W, I28F, and I28W, in which bulky amino acid side chains are introduced to block passageways between protein internal cavities or to fill these sites. Locations of these residues with respect to the heme group and xenon cavities 1, 2, and 4 are shown in Figure 1. In contrast to the situation in L29W MbCO, the spectral changes in the infrared bands upon CO migration between the cavities will be shown to be much more subtle than in mutants with aromatic side chains, such as mutants V68W (*24*), L29W (*25*), and L29Y/H64Q/T67R (*26*). Nevertheless, we were able to assign different photoproduct states to specific CO locations by studying the changes caused by mutation and Xe binding, in analogy to our work on L29W (*3*). These studies were complemented by flash photolysis experiments on MbCO and MbO_2 samples at ambient temperature. The similarities as well as the differences observed in the kinetic traces for different mutants and ligands can be understood well on the basis of the results of the FTIR−TDS experiments at cryogenic temperatures.

MATERIALS AND METHODS

Protein Expression and Purification. The plasmid pUC19 hosting the gene expressing recombinant "wild-type" sperm whale myoglobin was a kind gift from S. Sligar (University of Illinois at Urbana-Champaign). Site-directed mutagenesis was performed using the Quikchange mutagenesis kit (Stratagene Europe, Amsterdam, The Netherlands). Custom-designed primers were ordered from MWG (MWG-Biotech GmbH, Ebersberg, Germany). Mutant sperm whale myoglobins were expressed in *Escherichia coli* and purified as described previously (*27*).

Sample Preparation. For the IR experiments, the lyophilized protein was dissolved at a concentration of ~20 mM in cryosolvent [75% glycerol/25% potassium phosphate buffer (v/v, pH 8)], stirred under a CO atmosphere, and reduced with a sodium dithionite solution. The flash photolysis data were taken on dilute solutions in 3 cm × 1 cm × 1 cm sealed glass cuvettes. MbCO samples were prepared by dissolving the lyophilized protein in 100 mM sodium phosphate buffer (pH 8) to a final concentration of 10 μM, followed by reduction with excess sodium dithionite under a CO atmosphere. To obtain MbO_2 samples, a ferric myoglobin solution was reduced with dithionite. Excess reducing agent was removed by passing the solution through a Sephadex G25 column.

FTIR−TDS Experiments. To assess the rebinding properties of different photoproduct species in low-temperature experiments, temperature derivative spectroscopy (TDS) in the IR bands of the CO stretch was used. TDS is an experimental protocol designed to assess thermally activated rate processes with distributed barriers (*28*). It involves two sequential steps. In a first step, the sample is prepared by a specific illumination protocol that selectively populates the desired intermediate state(s). Subsequently, FTIR spectra are taken continuously while the temperature is increased linearly in time (typically at a rate of 5 mK/s) over a certain temperature interval. During this temperature ramp, FTIR spectra are collected continuously, one every kelvin. In the TDS analysis, absorbance difference spectra are calculated for successive temperatures. The change in the spectral area of an infrared band, $\Delta A(\nu,T)$, that occurs during acquisition of two successive spectra is assumed to be proportional to the change in the population of CO molecules, ΔN, contributing to the band. Population changes arise from ligand rebinding and ligand diffusion among different docking sites. Both of these processes are governed by thermal activation, and the temperature ramp protocol ensures that they occur sequentially with respect to the height of the activation enthalpy barrier. For a simple two-state reaction, the temperature axis can be converted to an enthalpy axis, with the barrier height approximately proportional to the ramp tem-

perature. We present TDS data as contour plots of the absorbance change on a surface spanned by the wavenumber and temperature axes, with solid (dotted) lines indicating increasing (decreasing) absorbance. Integration of the absorbance changes along the wavenumber axis yields the distribution of the rebinding ligands with respect to temperature (enthalpy barrier). The assumption implicit in this analysis, namely, that spectral changes are proportional to population changes, is only an approximation that has proven to be useful in many cases. In some experiments, however, the spectra exhibit a pronounced intrinsic temperature dependence (*29*), for which we need to account separately.

IR transmission spectra were collected between 1800 and 2400 cm^{-1} at a resolution of 2 cm^{-1} using an FTIR spectrometer equipped with an InSb detector (IFS 66v/S, Bruker, Karlsruhe, Germany). The sample solutions were kept between two CaF_2 windows (diameter of 25.4 mm) separated by a 75 μm thick Mylar washer and sandwiched inside a block of oxygen-free high-conductivity copper. This assembly was mounted on the coldfinger of a closed-cycle helium refrigerator (model SRDK-205AW, Sumitomo, Tokyo, Japan). A digital temperature controller (model 330, Lake Shore Cryotronics, Westerville, OH) allowed the temperature to be adjusted between 3 and 320 K. Photolysis was achieved with a continuous-wave, frequency-doubled Nd:YAG laser (model Forte 530-300, Laser Quantum, Manchester, U.K.), emitting an output power of ~300 mW at 532 nm.

Flash Photolysis. Samples were photolyzed using a 6 ns (full width at half-maximum) pulse from a frequency-doubled, Q-switched Nd:YAG laser (model Surelite II, Continuum, Santa Clara, CA). The ensuing absorbance changes were monitored at 436 nm using light from a tungsten source passed through a monochromator and the sample. The light intensity was measured with a photomultiplier tube (model R5600U, Hamamatsu, Middlesex, NJ) and recorded with a digital storage oscilloscope (model TDS 520, Tektronix) from 10 ns to 50 μs and a home-built logarithmic time-base digitizer (Wondertoy II) from 2 μs to 100 s. For every kinetic trace, 500 transients were averaged. For comparison of the kinetics from different samples, the measured absorbances were scaled to the peak Soret absorbance to account for slightly different sample concentrations and the difference in extinction coefficients of MbCO and MbO_2. Subsequently, normalization to a scale between 0 and 1 was achieved by setting the amplitude of solvent rebinding in wt MbCO to 0.96 (*30*). The kinetic traces were fitted with exponentials to obtain (pseudo-first-order) rate coefficients for recombination from the solvent.

RESULTS

FTIR Difference Spectra after a 1 s Illumination at 3 K. Figure 2 shows photolysis difference spectra in the regions of heme-bound and photodissociated CO for wt MbCO and various mutants. They were calculated from transmission spectra taken before and after a 1 s photolyzing illumination of the samples. The positions of all bands are compiled in Table 1. In Figure 2a, we compare the IR bands of wt MbCO and mutants I28F and I28W, which have modifications in the back of the distal pocket (Figure 1). In wt MbCO, we observe the dominant A_1 substate band at 1945 cm^{-1}, a smaller A_3 peak at 1930 cm^{-1}, and an additional tiny A_x band at 1970 cm^{-1}. This band appears at a higher pH, is not associated with a protonated H64 imidazole, and is therefore distinct from A_0 (*18*). Two pronounced bands at 2119 and 2131 cm^{-1} represent photoproduct states B_2 and B_1, respectively (*13*, *16*). Another small peak, B_0, is found at 2149 cm^{-1}. The spectra of the mutant samples are similar to those of wt MbCO, with slight changes in the relative fractions of the bands and the peak positions. In Figure 2b, the spectra of the I107W and L104W mutants are plotted together with the spectrum of wt MbCO. I107W has an altered Xe4 site, and L104W has a blocked Xe1 cavity (Figure 1). Whereas the spectrum of L104W resembles that of wt MbCO, I107W yields pronounced spectral differences. In this mutant, substates A_1 and A_3 are populated approximately equally, and the photodissociated CO ligands give rise to a broad spectrum with peaks at 2108 (B_2), 2129 (B_1), and 2152 cm^{-1} (B_0).

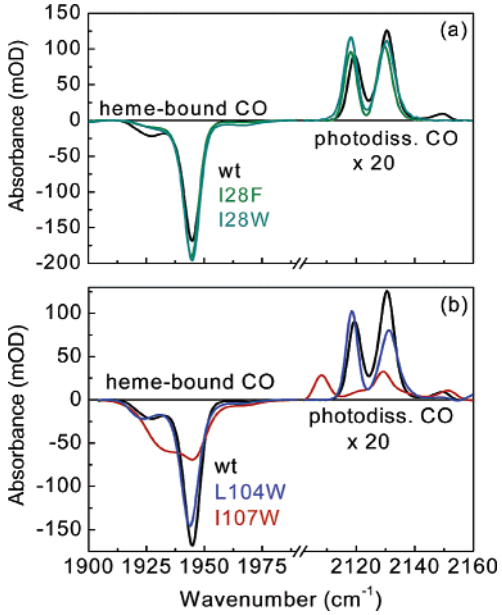

FIGURE 2: FTIR absorbance difference spectra of MbCO mutant samples (illumination for 1 s at 3 K) in the spectral regions of heme-bound and photodissociated CO: (a) wt, I28F, and I28W and (b) wt, I107W, and L104W.

Table 1: IR Band Positions of Heme-Bound and Photodissociated CO in Mutant Myoglobin Samples[a]

	pH[b]	A_1 (cm^{-1})	A_3 (cm^{-1})	A_x (cm^{-1})	B_1 (cm^{-1})	B_2 (cm^{-1})	B_0 (cm^{-1})
wt	7.0	1945	1930	1970	2131	2119	2149
I28F	7.6	1945	1929	–	2130	2118	–
I28W	7.6	1945	1929	–	2131	2118	–
L104W	7.3	1944	1932	1967	2131	2118	2149
I107W	7.2	1944	1933	–	2129	2108	2152

[a] Band positions were determined at 3 K, with an estimated experimental error of ±0.5 cm^{-1}. [b] The pH values were determined at room temperature with an accuracy of ±0.1 pH unit.

TDS following Brief Illumination at 3 K. To study migration and recombination of CO ligands in the various taxonomic substates, TDS experiments were performed after a 1 s illumination. In Figure 3, solid lines in the left column represent absorbance increases due to rebinding in the A substates. The contour plots of photodissociated CO in the heme pocket in the right column contain both solid and

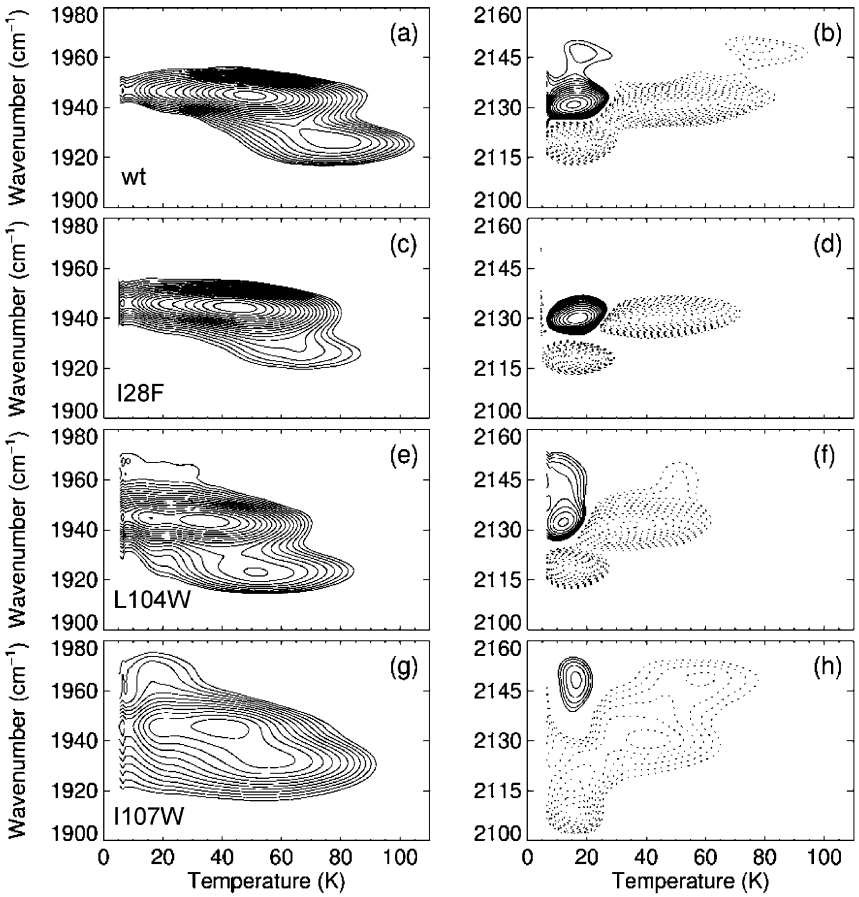

FIGURE 3: TDS contour maps of wt MbCO and mutants I28F, L104W, and I107W (illumination for 1 s at 3 K). Absorbance changes are shown for the IR bands of heme-bound CO (left column) and photolyzed CO (right column). Contours are spaced logarithmically; solid and dotted lines represent increasing and decreasing absorbance, respectively.

dashed contours. They denote, respectively, absorbance gain due to population transfer into a particular photoproduct state and absorbance loss due to population transfer out of a particular photoproduct state or, alternatively, rebinding. The TDS maps reveal similarities as well as subtle differences. For wt MbCO, recombination in A_1 peaks at 50 K and in A_3 at 78 K (Figure 3a). An exchange from B_2 at 2119 cm^{-1} to B_1 at 2131 cm^{-1} is represented by the occurrence of solid and dashed contours at the same temperature (Figure 3b). A solid contour at 2149 cm^{-1} and 18 K indicates a similar exchange process also for the population of intermediate B_0. This feature has not been observed in our earlier work because of insufficient dynamic range (*16*). Rebinding to A_1 occurs via photoproduct state B_1, whereas B_0 peaks at 78 K and is thus associated with A_3. The contour maps of the I28F mutant (Figure 3c,d) resemble those of wt MbCO. Here, recombination in A_1 peaks at 46 K and thus a bit lower than in wt MbCO. Because of the small fraction of A_3 rebinding at 70 K, a recombination signal from B_0 cannot be detected. For L104W (Figure 3e,f), significantly lower recombination temperatures are observed for taxonomic substates A_1 (35 K) and A_3 (51 K), which implies that the rebinding barriers at the heme iron are lower. The general features in the map of photodissociated CO are similar to those of wt MbCO (Figure 3f). For I107W, although the 3 K difference spectrum looked somewhat different from that of the other mutants (Figure 2b), the TDS maps again display the same overall features (Figure 3g,h). Rebinding from B_1 (2129 cm^{-1}) to substate A_1 peaks around 42 K, and rebinding from B_0 (2152 cm^{-1}) to A_3 peaks at 53 K. Furthermore, the photoproduct map exhibits an exchange at ~20 K involving the B_0 photoproduct state.

Extended Illumination Studies Probe Secondary Photoproducts in a Frozen Protein. Exposure to prolonged illumination with visible light enables ligands to migrate within the protein. In kinetic experiments, this process creates photoproduct intermediates with higher barriers opposing recombination (*6*, *7*, *24*). To conveniently survey these effects, MbCO samples were cooled under steady illumination from 160 to 3 K at a rate of 5 mK/s. Subsequently, an FTIR transmission spectrum was collected and referenced against a 3 K transmission spectrum taken without prior illumination. The resulting absorbance spectra differ markedly from those after a 1 s exposure at 3 K. Extended illumination does not produce any changes in the A substate bands (*15*, *16*) because large-scale protein motions are arrested below 160 K. Therefore, Figure 4 contains the spectra of the photolyzed ligands only. The top and bottom panels display the stretch bands after brief (1 s at 3 K) and extended (slow cooling from 160 to 3 K) illumination, respectively, normalized to equal areas of 1 OD cm^{-1} for better comparison. For wt MbCO, the magnitude of the B_2 band at 2119 cm^{-1} decreases upon extended illumination, and instead of B_1 at 2131 cm^{-1}, a new band appears at 2133 cm^{-1}. Whereas the photoproducts of mutants I28F and I28W after a 1 s illumination exhibit bands of the CO stretch almost identical to those of wt (Figure 4a), extended exposure to light produces markedly different spectra (Figure 4b). While

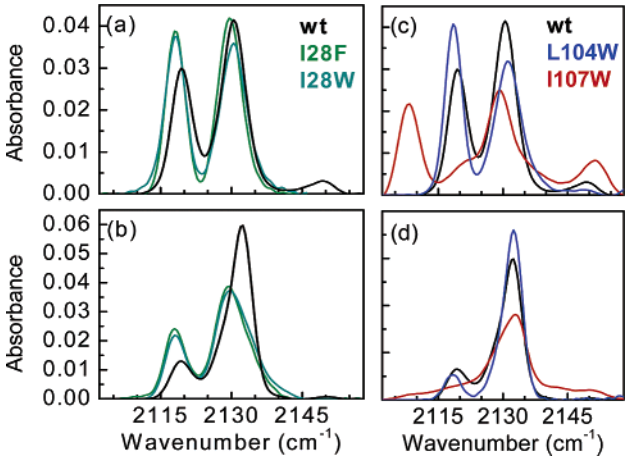

FIGURE 4: Photoproduct spectra of wt MbCO and mutants obtained with different illumination protocols. wt, I28F, and I28W: (a) illumination for 1 s at 3 K and (b) slow cooling from 160 to 3 K. wt, I107W, and L104W: (c) illumination for 1 s at 3 K and (d) slow cooling from 160 to 3 K under illumination. All spectra are shown normalized to equal areas of 1 OD cm^{-1}.

bands B_2 at 2118 cm^{-1} and B_1 at ~2130 cm^{-1} are still pronounced, a shoulder emerges on the high-frequency tail of B_1. In contrast to the 1 s photoproduct spectra (Figure 4c), I107W, L104W, and wt exhibit similar photoproduct spectra after extended illumination, with a predominant band at ~2133 cm^{-1} (Figure 4d). For wt and L104W, there is residual population in B_2 at 2119 cm^{-1}. In addition to the band at 2133 cm^{-1}, the spectrum of I107W exhibits a broad pedestal ranging from 2105 to 2155 cm^{-1}.

TDS experiments were performed to disperse these photoproduct signals according to their recombination temperatures. The data are presented as contour plots in Figure 5. In addition, we have plotted the integrated absorbances of the A_1 and A_3 substates as a function of temperature in Figure 6. For wt, the map of heme-bound CO (Figure 5a) shows three subpopulations rebinding to A_1 around 50, 80, and 115 K (see also Figure 6a). For A_3, two subpopulations with recombination maxima at 70 and 160 K can be discerned (Figures 5a and 6b). The corresponding photoproduct map (Figure 5b) displays a population transfer from a band at 2119 cm^{-1} to a doublet at 2131 and 2136 cm^{-1} below 25 K. Rebinding from the dominant photoproduct band at 2133 cm^{-1} to A_1 extends from 30 to 140 K, with no distinct change in the peak position up to 100 K. Afterward, the photoproduct band position shifts to slightly lower wavenumbers, as seen earlier with crystalline MbCO samples (*7*). An absorbance change is also visible near 2120 cm^{-1} in the temperature range of 50−120 K. Rebinding from B_0 to A_3 can be observed at 80 K, but no corresponding feature is resolved

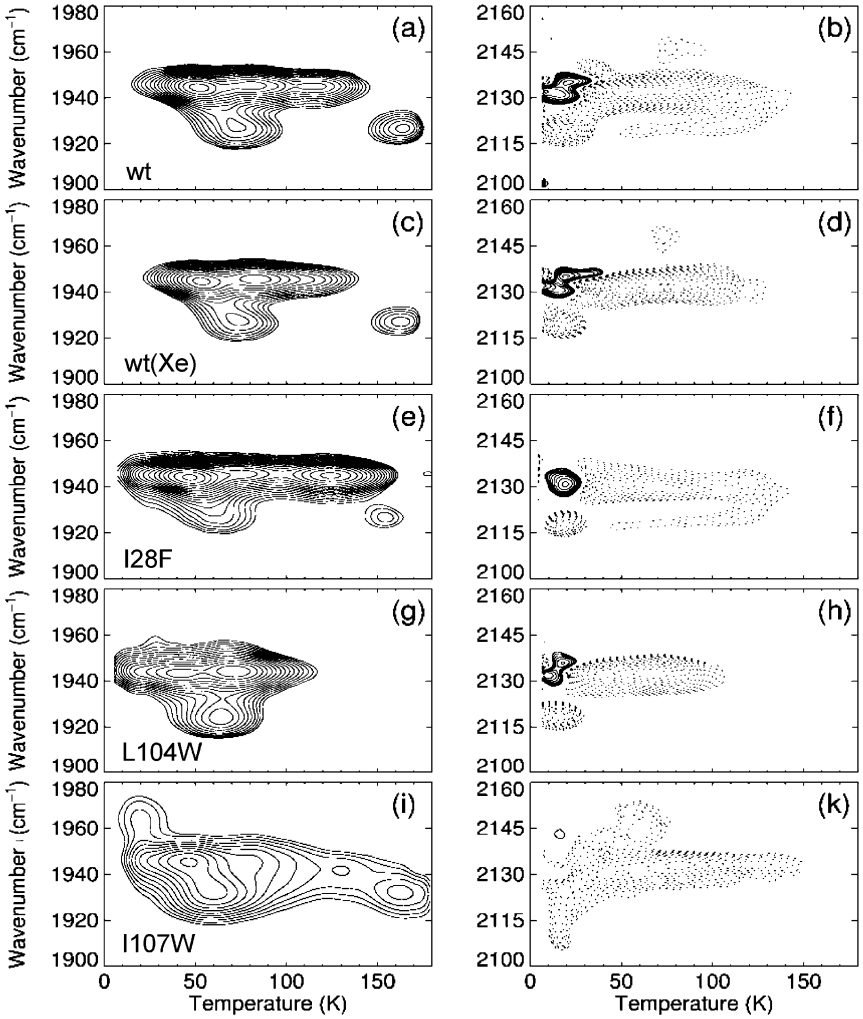

FIGURE 5: TDS contour maps of wt MbCO, wt(Xe), and related mutants I28F, L104W, and I107W taken after slow cooling under illumination from 160 to 3 K. Absorbance changes are shown for the IR bands of heme-bound CO (left column) and photolyzed CO (right column). Contours are spaced logarithmically; solid and dotted lines represent increasing and decreasing absorbance, respectively.

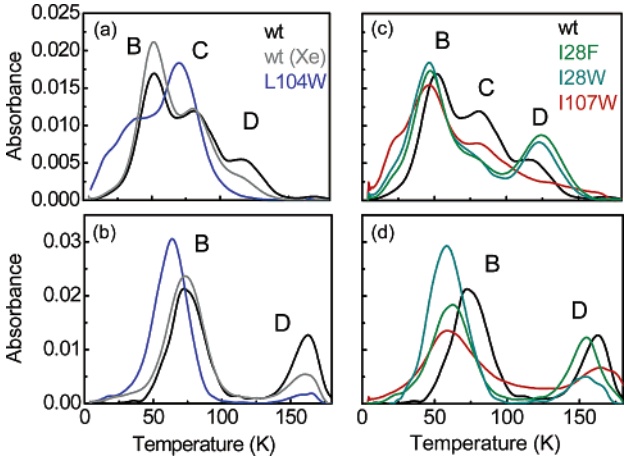

FIGURE 6: Integrated absorbance differences $\int \Delta A \, d\nu$ of substates A_1 (a and c) and A_3 (b and d) calculated from TDS data (Figure 5) and plotted as a function of temperature: (a and b) wt, wt(Xe), and L104W and (c and d) wt, I107W, I28F, and I28W.

for rebinding to A_3 at 160 K. Panels c and d of Figure 5 display the TDS maps of wt MbCO, equilibrated with 1 atm of Xe gas at 0 °C, denoted wt(Xe). Exposure of the sample was carried out so that Xe would bind in the internal cavities and at least partially prevent access of CO to one or more of them. In the A state map, almost identical features appear as for wt MbCO, except for a significant decrease in the subpopulations rebinding to substate A_1 at 115 K and substate A_3 at 160 K (Figures 5c and 6a,b). The map of the photoproducts (Figure 5d) is almost identical to the one of wt MbCO; the extended feature near 2120 cm^{-1}, however, is no longer present. In the TDS maps of mutant I28F, two subpopulations recombine to A_1 at 40 and 120 K (Figures 5e and 6c). Rebinding to A_3 occurs at 60 and 160 K (Figure 6d). The contour plot of photolyzed CO resembles that of wt. In L104W, only two subpopulations rebind to A_1, peaking at 40 and 70 K (Figures 5g and 6a). Rebinding to A_3 occurs around 65 K, somewhat higher than the temperature after a short illumination. The photoproduct map (Figure 5h) looks similar to that of wt. However, the stretched feature near 2120 cm^{-1} is again lacking. Major differences are seen in the contour plots of mutant I107W (Figure 5i,k). There is only a single well-resolved population rebinding to A_1 around 40 K, and at higher temperatures, the contours display a featureless tail (Figure 5i). In the integrated absorbance data in Figure 6c, a small peak at 80 K is still visible. The fraction of A_3 is much larger than for the other proteins and rebinds around 60 and 160 K. In contrast to the other samples, there is significant rebinding at temperatures between these two peaks. The photoproduct map (Figure 5k) displays a minor population transfer from a band at 2108 cm^{-1} to one at 2144 cm^{-1} around 15 K. Recombination in A_1 occurs from the band at 2131 cm^{-1} between 30 and 60 K. Above 70 K, this signal clearly shifts to 2134 cm^{-1}. Above 120 K, the band at 2134 cm^{-1} narrows considerably, and the shoulder at 2131 cm^{-1} vanishes.

Flash Photolysis at Ambient Temperature. To establish connections between FTIR spectroscopy of photoproduct intermediates at cryogenic temperatures and physiological ligand binding, flash photolysis data were collected at 20 °C on selected MbCO and MbO_2 mutant samples. All kinetic traces shown in Figure 7 display biphasic behavior, with a fast, nonexponential phase on the sub-microsecond scale,

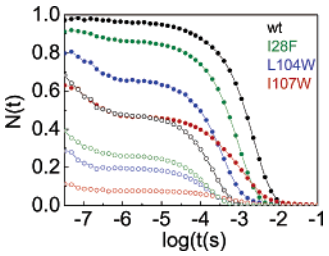

FIGURE 7: Flash photolysis kinetics of wt and related mutants monitored at 436 nm and 20 °C: (solid symbols) CO rebinding and (empty symbols) O_2 rebinding. Lines are shown to guide the eye.

Table 2: Comparison of the Bimolecular Rate Coefficients for CO and O_2 Binding to Sperm Whale Myoglobin[a]

	N_S(CO)	λ'_S(CO) (μM^{-1} s^{-1})	N_S(O_2)	λ'_S(O_2) (μM^{-1} s^{-1})
wt	0.96	0.56	0.47	16.20
I28F	0.86	0.95	0.25	19.90
L104W	0.65	2.20	0.19	19.90
I107W	0.47	0.56/2.2	0.80	18.00/3.10

[a] All data were recorded at 20 °C in 0.1 M sodium phosphate buffer (pH 8).

which arises from internal, geminate rebinding of ligands that did not manage to escape from the protein after photodissociation. The slower phase represents bimolecular rebinding. From these data, we extract two parameters by fitting a single exponential to the solvent process: (i) the amplitude of the solvent process (N_S), which represents the fraction of ligands that escape into the solvent after photodissociation, and (ii) the (pseudo-first-order) apparent rate coefficient λ_S for bimolecular rebinding from the solvent, which we have converted into second-order rate coefficients λ'_S using a CO concentration of 1 mM and an O_2 concentration of 1.34 mM in an aqueous solution. The parameters are compiled in Table 2.

In wt MbCO, ~96% of the photodissociated CO ligands escape from the protein after photodissociation at room temperature (*30*). In the mutant proteins, geminate rebinding is significantly enhanced, and the solvent amplitude N_S decreases in the following order: wt > I28F > L104W > I107W. Bimolecular CO binding in wt MbCO, I28F, and L104W is exponential, whereas that in I107W is markedly nonexponential.

The MbO_2 kinetics in Figure 7 show a significantly reduced amplitude of the solvent process, N_S, but the sequence of magnitudes for O_2 binding is the same as with CO. Also, the time course of geminate recombination extends out to ~1 μs. Bimolecular recombination is, however, significantly faster for MbO_2, with almost identical rate coefficients for the different mutants.

DISCUSSION

Primary Docking Site B. After a brief illumination at 3 K, we have obtained almost identical photoproduct spectra for the different mutants (Figure 2), except for I107W, which is the only mutant that was examined that contains an amino acid replacement in the vicinity of primary docking site B. Therefore, we infer that in all our samples photolyzed CO ligands settle in primary docking site B, located on top of pyrrol C (*8*, *9*, *31*). This underscores the crucial role of site B as the most easily accessible photoproduct state after

photodissociation (*32*, *33*). Even though ligand dissociation is driven by thermal energy and not by light in the physiological context, it is reasonable to assume that docking site B serves as a first transient CO storage site after bond rupture.

The IR experiments reveal a complexity of ligand dynamics that is hidden from the crystal structures. After a 1 s illumination at 3 K, a fraction of CO molecules (∼35% of all photolyzed ligands) reorients in docking site B at ∼15 K, as evidenced from a pairwise gain and loss of absorbance in two photoproduct bands (Figure 3, right column). For wt MbCO, the increase in the level of photoproduct B_1 at 2131 cm^{-1} that is accompanied by a decrease in the level of B_2 at 2119 cm^{-1} has been known for a long time (*13*). With improved data quality, we were able to see this effect for photoproduct band B_0, which is associated with the A_3 substate, for the first time (Figure 3b). B_0 gains population, but the band in which the corresponding loss occurs is not evident from the data. In a TDS experiment on an orthorhombic MbCO crystal sample, which had ∼90% of A_3 population, rebinding to A_3 was observed from photoproduct bands at 2131 and 2149 cm^{-1} (*16*). This observation may suggest that the missing partner is hidden underneath photoproduct B_1. Because A_1 is the dominant substate, its photoproduct state B_1 population should then increase much more due to the low-temperature exchange than the population of the missing partner of B_0 underneath B_1 decreases. Indeed, in the I107W mutant, with almost equal A_1 and A_3 populations, the two effects cancel, so there is no net increase in the level of B_1 at 2129 cm^{-1} (Figure 3h). The similar exchange in the photoproduct bands of A_3 and A_1 strongly suggests that both rebind CO from the B photoproduct state on top of the heme. The typically much higher enthalpy barrier of rebinding seen in A_3 is thus connected with an altered active site structure and not caused by a different CO location.

Secondary Ligand Docking Sites. The phenomenon that extended illumination enables ligands to sample longer-lived states at cryogenic temperatures was first noticed by Powers *et al.* (*34*) in 1987. In a detailed TDS study on wt MbCO in a glycerol/water mixture, we observed that discrete populations appear upon extended illumination that recombined at temperatures markedly higher than that of the normal low-temperature photoproduct (*6*). The absence of pronounced shifts in the IR bands of the photodissociated CO of MbCO in the glycerol/buffer cryosolvent led us to the initial interpretation that the CO stays in photoproduct state B, and that the long-lived states were caused by protein relaxation into a conformation with a higher rebinding barrier at the heme iron. Experiments with MbCO crystals revealed similar populations rebinding at higher temperatures, and clear shifts of the stretch bands of photodissociated CO between 100 and 130 K were observed and explained by ligand migration within the heme pocket (*7*). Unlike some mutants, for instance, L29W (*3*, *25*) and YQR (*26*), the wt protein shows only subtle shifts of the bands associated with photoproduct intermediates. However, despite the small shifts, CO ligands are not confined near the active site after dissociation, but migrate to more remote cavities, as shown here by using Xe and mutants with bulky side chains. The different subpopulations are best seen in the integrated absorbance data plotted in Figure 6. Depending on the mutant, conformation A_1 displays up to three recombining subpopulations and A_3 two at most. Within the A_1 substate, we assign the peak at ∼50 K to CO rebinding from docking site B, at ∼80 K from the Xe4 cavity (site C), and at ∼120 K from the Xe1 cavity (site D). The A_0 substate yields a similar temperature dependence of photoproducts (*6*); therefore, this assignment most likely holds for the A_0 conformation as well. The TDS peaks in A_3 are related to rebinding of CO from the primary photoproduct B (∼70 K) and from D/Xe1 (∼160 K). These assignments will be justified below.

Photoproduct D is assigned on the basis of the experiments with mutant L104W, in which the Xe1 cavity is completely blocked (*35*). Indeed, a subpopulation associated with photoproduct D does not appear in A_1 in this mutant upon extended illumination. For A_3, a weak feature is still visible around 160 K, indicative of an alternate location where a small fraction of CO ligands can also be stored. Supporting evidence comes from the data with Xe-bound wt MbCO. There, photodissociated ligands compete with Xe atoms for the internal cavities, and fewer CO ligands can migrate to secondary docking sites, as was shown in studies of geminate ligand binding by Scott *et al.* (*36*). With 1 atm of Xe gas, a noticeable effect should only occur for the cavity with the highest affinity for Xe, the Xe1 cavity (*37*). Indeed, panels a and b of Figure 6 show partial depletion (by ∼30%) of the high-temperature peaks associated with intermediate D for both A_1 and A_3. These results are also consistent with the X-ray structure analysis of horse heart MbCO crystals photolyzed at ∼160 K (*10*), which yielded a small fraction (∼20%) of photodissociated CO ligands in the proximal cavity Xe1.

In panels c and d of Figure 6, the integrated absorbance changes of mutants I107W, I28F, and I28W are compared with those of wt MbCO. For mutant I107W, with its bulky indole side chain hindering migration of CO to the back part of the distal pocket and further toward the proximal side (*38*), both intermediates C and D are significantly suppressed in A_1, as compared with wt MbCO, and rebinding from C and especially D is broadly distributed along the temperature axis (Figure 6c). For substate A_3, the population recombining from site D has decreased, and there is also a broad pedestal between the B and D features. This behavior agrees with our recent comparison of triple mutant YQR (L29Y/H64Q/T67R) and quadruple mutant YQRF (L29Y/H64Q/T67R/I107F) (*26*). In YQRF, the voluminous phenylalanine at position 107 plays a role similar to that of the tryptophan in I107W, and the TDS experiments revealed that escape of the ligand to the Xe4 cavity was indeed markedly hindered by F107. Molecular dynamics simulations also showed that residue 107 is situated along the passageway of ligands to site Xe4 and permits access to site Xe2 en route to site Xe1 (*38*).

The effect of extended illumination changes markedly when large aromatic residues are placed into the back of the Xe4 pocket. Mutants I28F and I28W display drastically lower occupancies of photoproduct C (Figure 6c), which suggests that these two side chains efficiently block the Xe4 cavity for CO. This observation strongly supports the assignment of C to an intermediate characterized by CO in the Xe4 pocket. A rather large fraction of CO ligands rebinds from site D in these mutants, however, at slightly higher temperatures than in wt MbCO. Apparently, a high yield of CO in

proximal cavity D is not correlated with a high yield of CO in site C. This was also seen with horse heart MbCO. There, only a very small fraction of ligands becomes trapped in site C, but site D is even more populated than in wt MbCO under identical illumination conditions (*6*). While it is tempting to argue from this observation that migration of the ligand from B to proximal cavity D does not necessarily occur sequentially via site C, we remark that migration pathways cannot be determined unambiguously with our techniques.

The assignment of light-induced photoproduct populations in the TDS maps to rebinding from the primary docking site B as well as from hydrophobic cavities Xe4 (C) and Xe1 (D) was based on their different rebinding temperatures (barriers). The IR stretch absorption of photolyzed CO is sensitive to the local environment of the CO molecule, especially the electric field (vibrational Stark effect) (*29*, *39*−*41*). Therefore, one expects that each CO location has its characteristic spectrum, as observed for mutants L29W (*3*, *5*, *25*) and YQR (*26*). The photoproduct TDS maps of wt MbCO in panels b and d of Figure 5, however, display pronounced spectral changes only for the CO exchange processes in photoproduct B. Ligand migration to secondary sites becomes apparent only by close inspection of the maps. Rebinding from photoproduct B is associated mainly with the band at 2131 cm^{-1}, which shifts slightly to ~2133 cm^{-1} as ligands return from the Xe4 site above ~60 K. Another small shift back to ~2129 cm^{-1} above 100 K signals the transition from C to D, as reported earlier for MbCO crystals (*7*). We also note in passing that the extended feature around 2120 cm^{-1} above 50 K in Figure 5b arises from the other twin in the CO doublet of photoproduct D. Incidentally, this is an example of an absorbance change arising from temperature-dependent motions of the CO in the Xe1 cavity, and not from rebinding (*29*). The small spectral changes for the CO in chemically different environments in intermediates B−D imply that the ligands experience similar local electric fields, as they are surrounded mainly by aliphatic and apolar residues. Only with mutants having aromatic substitutions, including V68F (*24*), L29W (*3*), and YQR (*26*), have we seen marked effects on the CO stretch frequencies, which apparently arise from the coupling of the CO dipole to the extended π-electron systems of these side chains.

Flash Photolysis at Room Temperature. The observation of CO migrating among different cavities in Mb after photodissociation at cryogenic temperatures raises the question of the relevance of this process for physiological ligand binding. Therefore, we have studied our mutants by flash photolysis at 20 °C (Figure 7). Kinetic data on ligand binding to Mb are typically modeled by introducing a set of intermediate species, which are represented by local minima on an enthalpy or free energy surface as a function of a reaction coordinate (Figure 8), as introduced by Austin *et al.* in 1975 (*42*). Of course, a one-dimensional (or lower-dimensional) description is an utterly simplistic representation of a protein−ligand system, considering the several thousand internal degrees of freedom of the protein and possibly multiple migration pathways of the ligand, associated with multiple reaction coordinates. Note that the scheme in Figure 8 is sequential, with bound state A, three geminate states B−D, and solvent state S. However, the Mb structure and experimental data suggest that the ligand may diffuse from solvent state S directly to B without necessarily passing through C and/or D. Another complication arises from the fact that the energy surfaces depend on external parameters such as temperature and viscosity (*43*). Furthermore, the A substates have their individual reaction surfaces, connected by protein fluctuations that induce transitions between the reaction surfaces (*15*, *44*, *45*).

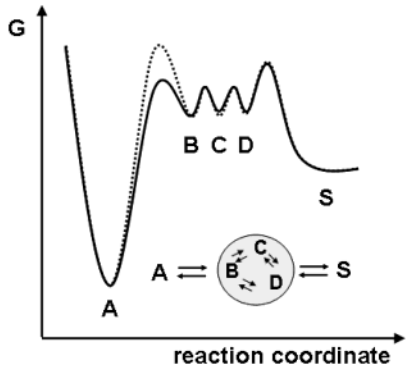

FIGURE 8: One-dimensional reaction surfaces describing binding of O_2 (—) and CO (···) to wt sperm whale Mb. The inset is a reaction scheme depicting the fast equilibration among internal docking sites B−D.

After these words of caution, we discuss our flash photolysis data on mutant MbCO and MbO_2 samples with the simple sequential scheme in Figure 8. The one-dimensional free energy surface for CO binding to Mb is characterized by an inner barrier (bond formation) and outer barrier (ligand entry and exit) that are assumed to be much larger than the internal barriers between geminate sites. The smaller interior barriers allow for fast equilibration among the geminate sites compared with both ligand binding and escape. After photodissociation, the ligands initially settle in state B. From there, they can either escape or rebind again by crossing the inner barrier. The time for recrossing the barrier can be estimated to be ~200 ns from the Arrhenius law, using the typical parameters, the enthalpy barrier for rebinding to the heme iron (H_{BA}, ~10 kJ/mol) and prefactor A_{BA} (~10^9 s^{-1}), determined from low-temperature flash photolysis (*42*, *46*, *47*). This result should be viewed as a rough estimate, considering that the inner barrier is heterogeneous. The time needed to cross the outer barrier is ~1 μs, as inferred from the fact that geminate rebinding extends out to this time. Thus, ligand exit from the protein is a comparatively slow process, as confirmed recently by time-resolved X-ray crystallography (*2*). In the X-ray data, photodissociated CO molecules were detected in two locations, at primary docking site B and at the Xe1 binding site in the proximal pocket. Approximately 100 ns after photolysis, all CO molecules still resided within the protein, in either of the two docking sites or bound to the heme.

Binding of CO at geminate locations B−D is governed by weak van der Waals interactions, and therefore, the enthalpies and free energies will be similar. Whenever secondary sites are available, the CO ligands inside the protein will spend only a small fraction of time on average in B, the only site through which bond formation can occur (*33*). Therefore, by fluctuating among states B−D, CO ligands have a much lower probability of binding, and the majority of them can take advantage of slow protein fluctuations that open exit channels into the solvent. Typi-

cally, ligands will shuttle back and forth many times among the geminate sites before exiting, and thus, the exact escape route remains obscure. Blocking access to the internal cavities increases the probability of CO residing in state B, and is, therefore, expected to enhance geminate rebinding. This effect is evident from Figure 7. When access to the Xe4 cavity by the bulky benzyl side chain in I28F is blocked, the geminate fraction N_I ($=1 - N_S$) increases from 4% in wt MbCO to 14% in I28F. In L104W, the Xe1 site is completely blocked, and thus, N_I equals 35%. I107W displays the largest geminate fraction (53%). Qualitatively, one can draw the following inferences from the geminate amplitudes. The Xe4 site does not appear to be all that important for assisting ligand escape, as indicated by the small geminate fraction of I28F. This observation also implies that the Xe1 site in I28F is accessible for transient CO storage, showing that CO migration does not follow a sequential B → C → D route. The importance of the Xe1 site is emphasized by the much larger geminate yield in the L104W mutant, in which ligands are confined to the distal heme side (*35*). Finally, in mutant I107W, most CO ligands rebind geminately because W107 is located in a strategic position, hindering ligand escape to both Xe1 and Xe4.

Further support for these conclusions comes from a comparison of the observed rate coefficients for rebinding from the solvent (λ_S). This quantity is given by a complicated expression that, in general, depends on all the relevant rate coefficients. For a three-well model with bound state A, photoproduct state B inside the protein, and solvent state S, a simple, approximate expression for λ_S can be obtained whenever the internal and solvent rebinding processes are clearly separated in time (*48*). In this approximation, λ_S is given by the product of three factors, k_{BA}, the rate coefficient for recombination from B to A, the pocket occupation factor P_B, which represents the equilibrium coefficient for binding CO at the geminate (B) site if there were no recombination at the heme iron, and N_S, the probability of ligand escape from the protein after dissociation from the heme iron

$$\lambda_S = k_{BA} P_B N_S = k_{BA} \frac{k_{SB}}{k_{BS}} \frac{k_{BS}}{k_{BA} + k_{BS}} \qquad (1)$$

This simple model can be extended to our case of multiple internal CO binding sites by assuming that the photolyzed CO molecules quasi-equilibrate among states B−D before either rebinding or exiting, as depicted by the shaded circle in the inset of Figure 8. For the rate coefficients, this assumption implies k_{BA}, k_{BS}, k_{CS}, and k_{DS} are much less than k_{BC}, k_{BD}, k_{CB}, and k_{DB}. As a consequence, states B−D can be treated formally as a single geminate state in a three-well model with bound state A, geminate state (B−D), and solvent state S. This "geminate" equilibrium, however, rescales the rate coefficient k_{BA} because it decreases the probability of CO residing at reactive site B. To account for this effect, an "internal" pseudoequilibrium factor $P_{B/CD}$ is introduced, defined as the equilibrium constant between state B and states C and D in the absence of binding or escape

$$k_{BA}' = k_{BA} P_{B/CD} = k_{BA} \frac{k_{CB} + k_{DB}}{k_{BC} + k_{BD}} \qquad (2)$$

With eq 2, ligand binding from the solvent can be approximated by eq 3, with the rate coefficient $\lambda_S(CO)$ given by

$$\lambda_S(CO) = k_{BA}' P_{BCD/S} N_S = k_{BA}' \frac{k_{SB} + k_{SC} + k_{SD}}{k_{BS} + k_{CS} + k_{DS}} \frac{k_{BS} + k_{CS} + k_{DS}}{k_{BA}' + k_{BS} + k_{CS} + k_{DS}} \qquad (3)$$

In eq 3, we have further introduced a modified pocket occupation factor $P_{BCD/S}$ that represents the overall equilibrium population at internal sites B−D with respect to solvent S (if no recombination would occur at the heme iron). N_S denotes the overall probability of CO exiting from one geminate site (B, C, or D). Of course, eq 3 reduces to the simple three-well model in eq 1, if sites C and D are not taken into account.

The expression for $\lambda_S(CO)$ raises the question of which of the three factors are responsible for the different properties of wt MbCO and the mutants. For wt MbCO and I28F, L104W, and I107W, only slightly different temperature dependencies are observed in the TDS data after a short illumination at 3 K (Figure 3), implying similar barriers at the heme iron and thus similar rate coefficients k_{BA}. This is not all that surprising because the mutations are not in the immediate vicinity of the active site (Figure 1). The solvent fraction N_S varies by a factor of ∼2 (0.47−0.96). Note that a decrease in N_S should translate into a decrease in $\lambda_S(CO)$. Exactly the opposite behavior is observed, however; the rate coefficients of the mutants with the lower bimolecular yields are larger. Consequently, the differences in $\lambda_S(CO)$ in these proteins have to be mainly attributed to different probabilities of CO occupation of site B.

Indeed, the observed changes in the solvent rates, $\lambda_S(CO)$, are consistent with the considerations presented above, which were based on the amplitudes of the solvent process, N_S. In I28F, solvent rebinding is faster by a factor of ∼2 than in wt MbCO because the Xe4 cavity is blocked for photolyzed ligands. This leaves only the Xe1 cavity as an alternate site, and therefore, the CO is forced to be in the reactive site B much longer on average. For L104W, λ_S is ∼4-fold larger than in wt MbCO. Because of the reduced amplitude N_S, we can estimate an ∼6-fold increase in the occupation of site B if the Xe1 cavity is removed. I107W exhibits an interesting, nonexponential bimolecular reaction even at room temperature. This indicates that subconformations exist in the deligated state (deoxy Mb) in this mutant with markedly different rebinding rates which do not interconvert on a time scale faster than milliseconds. A fit with two exponentials approximates the kinetics reasonably well. The nonexponential kinetics are likely connected to structural disorder of the W107 side chain. Unfortunately, there is no X-ray structure yet available for this mutant. In mutant YQRF, however, two conformations of the F107 side chain have been observed (*49*).

There are two ways in which W107 can cause drastic changes in the rebinding. We have already stated above that the large amplitude of geminate rebinding in I107W results from partial blockage of the migration pathways to the Xe4 and Xe1 cavities. Markedly different binding rates can also arise from different conformations blocking access to the cavities more or less severely. However, because W107 is close to the active site, it could also have an effect on the

inner barrier at the heme iron. In a comparison of YQR and YQRF mutant MbCOs, we have observed a decrease in the inner barrier in the dominant A_3 substate in YQRF, which was explained by the interaction of F107 with residue Q64 (*26*). Our oxygen binding data (*vide infra*) also support the notion that the nonexponential kinetics in I107W are caused by active site heterogeneity and not heterogeneous kinetics of ligand migration.

This comparison of mutants blocking internal cavities shows a combination of a decreasing N_S with an increasing λ_S upon blocking the Xe1 and Xe4 cavities, which is explained by assuming that the cavities act as transient storage sites, decreasing the probability of CO residing in site B. If the Xe cavities were crucial waystations on the entry−exit pathway, however, we would expect both drastically decreased N_S and λ_S values upon blocking these pathways. Apparently, other pathways dominate ligand migration to and from the solvent, such as the distal histidine gate, which opens when the imidazole side chain of H64 swings out of the heme pocket, as suggested by Olson and co-workers (*50*).

A comparison of the time traces of O_2- and CO-ligated samples (Figure 7) reveals similarities as well as obvious differences. Geminate rebinding of O_2 extends out to ∼1 μs, as for CO binding. This is a clear indication that the time scale of ligand exit is similar for the two ligands. The fraction of oxygen molecules that exit into the solvent after photodissociation is much smaller, 47% for wt MbO_2 instead of 96% for wt MbCO. Remarkably, the sequence in which N_S decreases for the different samples is identical for CO and O_2. In light of our previous discussion, this observation suggests that the cavities play a similar role for O_2 and CO ligands. The difference in the kinetics between CO and O_2 appears to be a significantly lower inner barrier for O_2 than for CO, so the probability of rebinding from site B is markedly enhanced. It is generally accepted that the quantum yield for NO, O_2, and CO photodissociation is unity, but there are two different ways by which O_2 rebinds to Mb. A fast, essentially barrier-less fraction rebinds on the picosecond time scale at room temperature (*51*−*53*). Even at low temperatures (∼4 K), this fraction is so fast that it cannot be observed in nanosecond flash photolysis experiments (*43*). The slow fraction exhibits kinetic properties at low temperatures that are similar to those of MbCO (*42*, *54*−*56*). The structural reasons for these pronounced differences are not yet clear. Miller *et al.* (*57*) have suggested that the fast and slow populations differ in their proximal environments, with a more planar heme configuration in the photoproduct of the fast states. At room temperature, one may expect that slow and fast conformations interconvert on the time scale of our kinetic experiments so that the average inner barrier for O_2 becomes significantly smaller than for CO. In wt MbO_2, more than 30% of the ligands have rebound before we could even take the first data point at 30 ns. The ensuing decay of the geminate phase indicates that the O_2 ligands shuttle back and forth among the cavities out to ∼1 μs, as in MbCO, while some rebind and some finally escape into the solvent. It is clear that removal of the internal docking sites in the mutants causes even more enhanced geminate rebinding, resulting in a smaller N_S.

A small solvent process amplitude also means that ligands, upon re-entry of the protein from the solvent, will predominantly rebind and not escape again. In other words, ligand binding is governed by the outer barrier, and our reaction surface in Figure 8, which we had effectively reduced to a three-well model in the case of CO binding, then simplifies even further to a two-well model. It is easy to see that, for large k_{BA} values, eq 3 yields

$$\lambda_S = k_{SB} + k_{SC} + k_{SD} \quad (4)$$

which is the sum of all rate coefficients associated with ligand entry. Hence, the outer barrier governs O_2 recombination, and details of the inner machinery of the protein should become irrelevant. Indeed, the quantitative analysis of the time courses of MbO_2 samples wt, I28F, L104W, and I107W yields essentially identical values of $\lambda_S(O_2)$ within the experimental error (Table 2). This implies that entry−exit pathways through C and D, which are kinetically of minor relevance for CO binding, are not important for O_2 binding either, so $\lambda_S(O_2) \sim k_{SB}$. In their study of oxygen binding in a large variety of mutant Mbs, Scott *et al.* (*50*) suggested that the globin acts like a baseball glove that "catches" and then traps incoming ligands long enough to allow bond formation with the heme iron. In this model, filling the glove with large amino acid side chains makes it more difficult to catch incoming ligands. The results presented here emphasize not only that the volume of the heme pocket is important but also that docking site B plays a crucial role in capturing ligands. As long as this site is available, ligands entering the protein will be trapped efficiently. However, when aromatic residues are introduced into the distal pocket that interfere sterically with the primary docking site, e.g., in V68W or L29W (*3*), the efficiency of capturing ligands is markedly reduced.

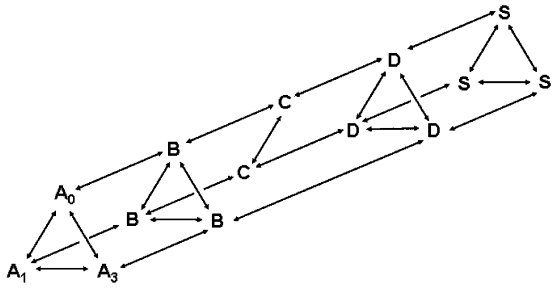

FIGURE 9: Scheme of the three ligand-bound conformations of sperm whale Mb, A_0, A_1, and A_3, and their associated reaction intermediates. For details, see the text.

CONCLUSIONS

FTIR−TDS experiments on sperm whale MbCO enabled us to identify a small number of reaction intermediates, associated with CO ligands residing in different internal cavities of myoglobin at cryogenic temperatures. Figure 9 shows a scheme of the three ligand-bound conformations of sperm whale Mb, A_0, A_1, and A_3, and their associated reaction intermediates.

State B is characterized by ligands at the primary docking site, from which formation of the heme iron−ligand bond occurs. In C and D, ligands are located in the Xe4 and Xe1 cavities, respectively. Interestingly, state C does not exist in the A_3 conformation. The deligated state is represented by S. Below 160 K, large-scale protein motions are frozen in,

and transitions between photolysis intermediates are observed separately within the A_0, A_1, and A_3 conformations. Above 160 K, transitions between A substates and their associated reaction intermediates can occur. We emphasize here that the scheme in Figure 9 is *not* meant to imply that ligands must migrate sequentially through *all* intermediates on their way from the solvent to the active site. For instance, they may rebind directly via the S → B → A route without visiting the Xe4 or Xe1 cavity.

Via a combination of the FTIR−TDS data at cryogenic temperature with flash photolysis results for MbCO and MbO_2 at room temperature, the following picture has emerged, which emphasizes the importance of both protein and ligand dynamics in the binding reaction: within picoseconds of dissociation from the heme iron, ligands move to a specific docking site B in the distal heme pocket, which plays a key role in formation of the iron−ligand bond. This site is engineered such that ligands can reside there for long times (nanoseconds) without rebinding. Ligands shuttle back and forth between primary docking site B and secondary sites C and D, which reduces their probability of rebinding while they wait for large-scale protein fluctuations on nanosecond to microsecond time scales that open exit channels through which the ligands finally escape from the protein. Our results have shown that this scenario holds for both CO and O_2 ligands. The key difference between the two ligands is that the inner barrier is markedly reduced for O_2, and as a result, the internal cavities only control the probability of ligand escape, but not the association rate for oxygen binding.

ACKNOWLEDGMENT

We thank Uwe Theilen for constructing and producing the myoglobin mutants used in this study. We are indebted to Dr. Don C. Lamb for discussions and technical assistance in the early stages of this investigation.

REFERENCES

1. Srajer, V., Teng, T., Ursby, T., Pradervand, C., Ren, Z., Adachi, S., Schildkamp, W., Bourgeois, D., Wulff, M., and Moffat, K. (1996) Photolysis of the carbon monoxide complex of myoglobin: nanosecond time-resolved crystallography, *Science 274*, 1726−1729.
2. Srajer, V., Ren, Z., Teng, T. Y., Schmidt, M., Ursby, T., Bourgeois, D., Pradervand, C., Schildkamp, W., Wulff, M., and Moffat, K. (2001) Protein conformational relaxation and ligand migration in myoglobin: a nanosecond to millisecond molecular movie from time-resolved Laue X-ray diffraction, *Biochemistry 40*, 13802−13815.
3. Nienhaus, K., Deng, P., Kriegl, J. M., and Nienhaus, G. U. (2003) Structural Dynamics of Myoglobin: Spectroscopic and Structural Characterization of Ligand Docking Sites in Myoglobin Mutant L29W, *Biochemistry 42*, 9633−9646.
4. Li, T., Quillin, M. L., Phillips, G. N., Jr., and Olson, J. S. (1994) Structural determinants of the stretching frequency of CO bound to myoglobin, *Biochemistry 33*, 1433−1446.
5. Ostermann, A., Waschipky, R., Parak, F. G., and Nienhaus, G. U. (2000) Ligand binding and conformational motions in myoglobin, *Nature 404*, 205−208.
6. Nienhaus, G. U., Mourant, J. R., Chu, K., and Frauenfelder, H. (1994) Ligand binding to heme proteins: the effect of light on ligand binding in myoglobin, *Biochemistry 33*, 13413−13430.
7. Nienhaus, G. U., Chu, K., and Jesse, K. (1998) Structural heterogeneity and ligand binding in carbonmonoxy myoglobin crystals at cryogenic temperatures, *Biochemistry 37*, 6819−6823.
8. Teng, T. Y., Srajer, V., and Moffat, K. (1994) Photolysis-induced structural changes in single crystals of carbonmonoxy myoglobin at 40 K, *Nat. Struct. Biol. 1*, 701−705.
9. Schlichting, I., Berendzen, J., Phillips, G. N., Jr., and Sweet, R. M. (1994) Crystal structure of photolysed carbonmonoxy-myoglobin, *Nature 371*, 808−812.
10. Chu, K., Vojtchovsky, J., McMahon, B. H., Sweet, R. M., Berendzen, J., and Schlichting, I. (2000) Structure of a ligand-binding intermediate in wild-type carbonmonoxy myoglobin, *Nature 403*, 921−923.
11. Shimada, H., and Caughey, W. S. (1982) Dynamic protein structures. Effects of pH on conformer stabilities at the ligand-binding site of bovine heart myoglobin carbonyl, *J. Biol. Chem. 257*, 11893−11900.
12. Fuchsman, W. H., and Appleby, C. A. (1979) CO and O_2 complexes of soybean leghemoglobins: pH effects upon infrared and visible spectra. Comparisons with CO and O_2 complexes of myoglobin and hemoglobin, *Biochemistry 18*, 1309−1321.
13. Alben, J. O., Beece, D., Bowne, S. F., Doster, W., Eisenstein, L., Frauenfelder, H., Good, D., McDonald, J. D., Marden, M. C., Moh, P. P., Reinisch, L., Reynolds, A. H., Shyamsunder, E., and Yue, K. T. (1982) Infrared spectroscopy of photodissociated carboxy-myoglobin at low temperatures, *Proc. Natl. Acad. Sci. U.S.A. 79*, 3744−3748.
14. Ansari, A., Berendzen, J., Braunstein, D., Cowen, B. R., Frauenfelder, H., Hong, M. K., Iben, I. E., Johnson, J. B., Ormos, P., Sauke, T. B., *et al.* (1987) Rebinding and relaxation in the myoglobin pocket, *Biophys. Chem. 26*, 337−355.
15. Johnson, J. B., Lamb, D. C., Frauenfelder, H., Müller, J. D., McMahon, B., Nienhaus, G. U., and Young, R. D. (1996) Ligand binding to heme proteins. VI. Interconversion of taxonomic substates in carbonmonoxymyoglobin, *Biophys. J. 71*, 1563−1573.
16. Mourant, J. R., Braunstein, D. P., Chu, K., Frauenfelder, H., Nienhaus, G. U., Ormos, P., and Young, R. D. (1993) Ligand binding to heme proteins: II. Transitions in the heme pocket of myoglobin, *Biophys. J. 65*, 1496−1507.
17. Braunstein, D. P., Chu, K., Egeberg, K. D., Frauenfelder, H., Mourant, J. R., Nienhaus, G. U., Ormos, P., Sligar, S. G., Springer, B. A., and Young, R. D. (1993) Ligand binding to heme proteins: III. FTIR studies of His-E7 and Val-E11 mutants of carbonmonoxymyoglobin, *Biophys. J. 65*, 2447−2454.
18. Müller, J. D., McMahon, B. H., Chien, E. Y., Sligar, S. G., and Nienhaus, G. U. (1999) Connection between the taxonomic substates and protonation of histidines 64 and 97 in carbonmonoxy myoglobin, *Biophys. J. 77*, 1036−1051.
19. Kushkuley, B., and Stavrov, S. S. (1996) Theoretical study of the distal-side steric and electrostatic effects on the vibrational characteristics of the FeCO unit of the carbonylheme proteins and their models, *Biophys. J. 70*, 1214−1229.
20. Kushkuley, B., and Stavrov, S. S. (1997) Theoretical study of the electrostatic and steric effects on the spectroscopic characteristics of the metal−ligand unit of heme proteins. 2. C−O vibrational frequencies, ^{17}O isotropic chemical shifts, and nuclear quadrupole coupling constants, *Biophys. J. 72*, 899−912.
21. Yang, F., and Phillips, G. N., Jr. (1996) Crystal structures of CO-, deoxy- and met-myoglobins at various pH values, *J. Mol. Biol. 256*, 762−774.
22. Tian, W. D., Sage, J. T., and Champion, P. M. (1993) Investigations of ligand association and dissociation rates in the "open" and "closed" states of myoglobin, *J. Mol. Biol. 233*, 155−166.
23. Vojtechovsky, J., Chu, K., Berendzen, J., Sweet, R. M., and Schlichting, I. (1999) Crystal structures of myoglobin-ligand complexes at near-atomic resolution, *Biophys. J. 77*, 2153−2174.
24. Nienhaus, K., Lamb, D. C., Deng, P., and Nienhaus, G. U. (2002) The Effect of Ligand Dynamics on Heme Electronic Transition Band III in Myoglobin, *Biophys. J. 82*, 1059−1067.
25. Nienhaus, G. U., and Nienhaus, K. (2002) Infrared Study of Carbon Monoxide Migration among Internal Cavities of Myoglobin Mutant L29W, *J. Biol. Phys. 28*, 163−172.
26. Lamb, D. C., Nienhaus, K., Arcovito, A., Draghi, F., Miele, A. E., Brunori, M., and Nienhaus, G. U. (2002) Structural Dynamics of Myoglobin. Ligand Migration studied by Fourier Transform Infrared/Temperature Derivative Spectroscopy, *J. Biol. Chem. 277*, 11636−11644.
27. Springer, B. A., and Sligar, S. G. (1987) High-level expression of sperm whale myoglobin in *Escherichia coli*, *Proc. Natl. Acad. Sci. U.S.A. 84*, 8961−8965.

28. Berendzen, J., and Braunstein, D. (1990) Temperature-derivative spectroscopy: a tool for protein dynamics, *Proc. Natl. Acad. Sci. U.S.A. 87*, 1−5.
29. Kriegl, J. M., Nienhaus, K., Deng, P., Fuchs, J., and Nienhaus, G. U. (2003) Ligand Dynamics in a Protein Internal Cavity, *Proc. Natl. Acad. Sci. U.S.A. 100*, 7069−7074.
30. Henry, E. R., Sommer, J. H., Hofrichter, J., and Eaton, W. A. (1983) Geminate recombination of carbon monoxide to myoglobin, *J. Mol. Biol. 166*, 443−451.
31. Hartmann, H., Zinser, S., Komninos, P., Schneider, R. T., Nienhaus, G. U., and Parak, F. (1996) X-ray structure determination of a metastable state of carbonmonoxy myoglobin after photodissociation, *Proc. Natl. Acad. Sci. U.S.A. 93*, 7013−7016.
32. Lim, M., Jackson, T. A., and Anfinrud, P. A. (1995) Binding of CO to myoglobin from a heme pocket docking site to form nearly linear Fe−C−O, *Science 269*, 962−966.
33. Lim, M., Jackson, T. A., and Anfinrud, P. A. (1997) Ultrafast rotation and trapping of carbon monoxide dissociated from myoglobin, *Nat. Struct. Biol. 4*, 209−214.
34. Powers, L., Chance, B., Chance, M., Campbell, B., Friedman, J., Khalid, S., Kumar, C., Naqui, A., Reddy, K. S., and Zhou, Y. (1987) Kinetic, structural, and spectroscopic identification of geminate states of myoglobin: a ligand binding site on the reaction pathway, *Biochemistry 26*, 4785−4796.
35. Liong, E. C., Dou, Y., Scott, E. E., Olson, J. S., and Phillips, G. N., Jr. (2001) Waterproofing the heme pocket. Role of proximal amino acid side chains in preventing hemin loss from myoglobin, *J. Biol. Chem. 276*, 9093−9100.
36. Scott, E. E., and Gibson, Q. H. (1997) Ligand migration in sperm whale myoglobin, *Biochemistry 36*, 11909−11917.
37. Tilton, R. F., Jr., Kuntz, I. D., Jr., and Petsko, G. A. (1984) Cavities in proteins: structure of a metmyoglobin-xenon complex solved to 1.9 Å, *Biochemistry 23*, 2849−2857.
38. Elber, R., and Karplus, M. (1990) Enhanced Sampling in Molecular Dynamics: Use of the Time-Dependent Hartree Approximation for a Simulation of Carbon Monoxide Diffusion through Myoglobin, *J. Am. Chem. Soc. 112*, 9161−9175.
39. Phillips, G. N., Jr., Teodoro, M. L., Li, T., Smith, B., and Olson, J. S. (1999) Bound CO is a molecular probe of electrostatic potential in the distal pocket of myoglobin, *J. Phys. Chem. B 103*, 8817−8829.
40. Bublitz, G. U., and Boxer, S. G. (1997) Stark spectroscopy: applications in chemistry, biology, and materials science, *Annu. Rev. Phys. Chem. 48*, 213−242.
41. Park, E. S., and Boxer, S. G. (2002) Origins of the sensitivity of molecular vibrations on electric fields: Carbonyl and Nitrosyl Stretches in Model Compounds and Proteins, *J. Phys. Chem. B 106*, 5800−5806.
42. Austin, R. H., Beeson, K. W., Eisenstein, L., Frauenfelder, H., and Gunsalus, I. C. (1975) Dynamics of ligand binding to myoglobin, *Biochemistry 14*, 5355−5373.
43. Beece, D., Eisenstein, L., Frauenfelder, H., Good, D., Marden, M. C., Reinisch, L., Reynolds, A. H., Sorensen, L. B., and Yue, K. T. (1980) Solvent viscosity and protein dynamics, *Biochemistry 19*, 5147−5157.
44. Young, R. D., Frauenfelder, H., Johnson, J. B., Lamb, D. C., Nienhaus, G. U., Phillip, R., and Scholl, R. (1991) Time and temperature dependence of large-scale conformational transitions in myoglobin, *Chem. Phys. 158*, 315−328.
45. Zhu, L., Sage, J. T., Rigos, A. A., Morikis, D., and Champion, P. M. (1992) Conformational interconversion in protein crystals, *J. Mol. Biol. 224*, 207−215.
46. McMahon, B. H., Stojkovic, B. P., Hay, P. J., Martin, R. L., and García, A. E. (2000) Microscopic model of carbon monoxide binding to myoglobin, *J. Chem. Phys. 113*, 6831−6850.
47. Steinbach, P. J., Ansari, A., Berendzen, J., Braunstein, D., Chu, K., Cowen, B. R., Ehrenstein, D., Frauenfelder, H., Johnson, J. B., Lamb, D. C., *et al.* (1991) Ligand binding to heme proteins: connection between dynamics and function, *Biochemistry 30*, 3988−4001.
48. Doster, W., Beece, D., Bowne, S. F., DiIorio, E. E., Eisenstein, L., Frauenfelder, H., Reinisch, L., Shyamsunder, E., Winterhalter, K. H., and Yue, K. T. (1982) Control and pH dependence of ligand binding to heme proteins, *Biochemistry 21*, 4831−4939.
49. Draghi, F., Miele, A. E., Travaglini-Allocatelli, C., Vallone, B., Brunori, M., Gibson, Q. H., and Olson, J. S. (2002) Controlling ligand binding in myoglobin by mutagenesis, *J. Biol. Chem. 277*, 7509−7519.
50. Scott, E. E., Gibson, Q. H., and Olson, J. S. (2001) Mapping the pathways for O_2 entry into and exit from myoglobin, *J. Biol. Chem. 276*, 5177−5188.
51. Petrich, J. W., Poyart, C., and Martin, J. L. (1988) Photophysics and reactivity of heme proteins: a femtosecond absorption study of hemoglobin, myoglobin, and protoheme, *Biochemistry 27*, 4049−4060.
52. Petrich, J. W., Lambry, J. C., Kuczera, K., Karplus, M., Poyart, C., and Martin, J. L. (1991) Ligand binding and protein relaxation in heme proteins: a room-temperature analysis of NO geminate recombination, *Biochemistry 30*, 3975−3987.
53. Chance, M. R., Courtney, S. H., Chavez, M. D., Ondrias, M. R., and Friedman, J. M. (1990) O_2 and CO reactions with heme proteins: quantum yields and geminate recombination on picosecond time scales, *Biochemistry 29*, 5537−5545.
54. Tetreau, C., Novikov, E., Tourbez, M., and Lavalette, D. (2002) Kinetic evidence for three photolyzable taxonomic conformational substates in oxymyoglobin, *Biophys. J. 82*, 2148−2155.
55. Frauenfelder, H., and Wolynes, P. G. (1985) Rate theories and puzzles of hemeprotein kinetics, *Science 229*, 337−345.
56. Nienhaus, G. U., Chu, K., McMahon, B., and Müller, J. D. (1995) Conformational Relaxation and Ligand Binding in Heme Proteins, in *Proceedings of the Ninth Conversation in Biomolecular Stereodynamics* (Sarma, R. S., and Sarma, M. H., Eds.) State University of New York, Albany, NY.
57. Miller, L. M., Patel, M., and Chance, M. R. (1996) Identification of Conformational Substates in Oxymyoglobin through the pH-Dependence of the Low-Temperature Photoproduct Yield, *J. Am. Chem. Soc. 118*, 4511−4517.

BI034788K